The effect of flow stratification on ship performance: a numerical study

Patrick Reid, Momchil Terziev, Tahsin Tezdogan & Atilla Incecik

Published online: 22 Feb 2024.

Submit your article to this journal

View related articles

View Crossmark data

Taylor & Francis
Taylor & Francis Group

The effect of flow stratification on ship performance: a numerical study

Patrick Reid[a], Momchil Terziev [b], Tahsin Tezdogan [c] and Atilla Incecik [b]

[a]Department of Naval Architecture, Ocean and Marine Engineering, University of Strathclyde, Glasgow, UK; [b]Faculty of Engineering, University of Strathclyde, Glasgow, UK; [c]Department of Civil, Maritime and Environmental Engineering, University of Southampton, Southampton, UK

ABSTRACT

If a layer of low-density water settles on top of higher density water, such as fresh water melting from a glacier and settling on top of colder seawater, a body of water can stratify into stable, distinct layers. A vessel advancing in such a stratified fluid can generate internal waves between these layers. The generation of internal waves requires energy and thus increases the resistance experienced by the vessel, a phenomenon known as the dead water effect which can result in a severe reduction in speed and loss of steering power. This study uses Computational Fluid Dynamics (CFD) to investigate the increase in ship resistance caused by the dead water effect. The results show that the presence of a stratified flow can increase total resistance approximately sixfold in extreme conditions. At standard operating conditions, total resistance may increase by approximately 6% as a result of flow stratification.

1. Introduction

When sailing in a calm ocean, ships produce a characteristic V-shaped wave pattern, emanating from the bow at the so-called Kelvin half-angle of approximately 19.47⁰. That distinctive wave pattern is only produced on a calm ocean; the presence of waves or currents modify the apparent wake considerably (Ellingsen and Brevik 2014; Li et al. 2019). Similarly, under certain conditions a calm ocean may stratify into layers of fresh and saltwater forming an interface in which a second, internal wave system, may be generated by the passage of a ship. Such stratification, the internal wave system generated by the ship and its effects of power consumption is known as the dead water effect.

Dead water can cause severe loss in performance with recorded examples documenting ships slowing from 6–7 knots to 1.5 knots (Walker 1991). While these effects are severe the conditions required for the dead water effect occur are rare and have not created major obstacles for seafaring. However, as climate change continues to worsen glaciers are likely to melt a greater amount of fresh water into the ocean (Nesje et al. 2008). As glacial runoff is one of the easiest ways for a stable stratification of two distinct layers to form (Grue 2018) the dead water effect may become increasingly common. In addition, climate change is expected to increase the likelihood of the pycnocline ocean layer being present at the ocean's surface (Sallée et al. 2021). This will increase the likelihood of ships experiencing increased resistance due to linear stratification as described by Mercier et al. (2011).

The present study reported in this paper aims to understand the effect of flow stratification on the performance of a modern container ship. To do this it is necessary to investigate the types of flow stratification that occur in nature and to determine which scenarios pose a risk of affecting ship performance. A Reynolds Averaged Navier-Stokes (RANS) methodology is adopted to model several scenarios, including the design speed as well as a case where the greatest increase in resistance would be expected based on existing theoretical research. The latter is used to quantify the maximum increase in resistance that can occur due to flow stratification and to break the resistance down into its components of pressure and friction.

The remainder of this paper is arranged as follows. Section 2 provides background information and a review of the existing literature regarding flow stratification, naturally occurring dead water, internal waves, and the dead water effect. Section 3 outlines the geometry and case studies. Section 4 describes the numerical modelling process performed using CFD. Following this, section 5 covers the analysis of the simulation results and is split into multiple subsections. Finally, section 6 contains the concluding remarks and sets out recommendations for future work.

2. Background

Flow stratification is a phenomenon that occurs to some extent in any large body of water. A fluid can be said to be stratified if the fluid density varies with distance in any direction. However, stable stratification can only occur for a vertically stratified fluid (Esmaeilpour 2017).

When describing a stratified fluid there are two primary parameters that determine whether a stratification will be stable or not. The first of these is the Brunt-Vaisala frequency, which can be thought of as the frequency of an infinitesimal fluid element as it oscillates up and down in a vertical density gradient (Gill 1982). As the volume moves downwards it will become surrounded by fluid of a higher density which will result in the fluid being pushed back up by the force of buoyancy. As it moves upwards its momentum will cause to move through the region of equal density and become surrounded by lower density fluid, causing it to be pushed back down as its weight overcomes the buoyancy force. The frequency of this oscillation is given by (Wüest and Lorke 2003):

$$N^2 = -\frac{g}{\rho}\frac{\partial \rho}{\partial z} \qquad (1)$$

where N is the Brunt-Vaisala frequency, $\partial\rho/\partial z$ is the vertical density gradient, g is the acceleration due to gravity, and ρ is the density at depth z. In the context of a stratified flow, as long as $N^2 > 0$ the fluid element will oscillate stably with frequency N until damped to zero by viscous forces, resulting in a stable stratification. If $N < 0$ the oscillations will continue to grow until the two strata of fluid mix. It is also important to note that internal waves will only be generated within a stratified fluid if the disturbance is at a frequency that is less than the Brunt-Vaisala frequency (Gill 1982).

The second main parameter required for stable stratification is the Richardson number (Ri), this is defined as (Nappo 2012):

$$Ri = N^2/(\partial u/\partial z)^2 \qquad (2)$$

where $\partial u/\partial z$ is the vertical shear velocity. The Richardson number represents the ratio of turbulence kinetic energy created by buoyant forces to turbulent kinetic energy produced by shear forces (Schnelle 2003). The flow will be stable as long as the Richardson number is higher than 0.25 however if $0 < Ri < 0.25$ Kelvin-Helmholtz waves will appear and cause the flow to become turbulent (Drazin 1970). For Richardson numbers of $Ri < 0$ the flow will be convectively unstable, meaning that it will become turbulent even in the absence of an initial disturbance (Nappo 2012).

2.1. Naturally occurring dead water

The specific case of flow stratification being investigated herein is the 'dead water effect' a phenomenon that creates an increase in the resistance of a body moving in a stable, distinctly stratified fluid, due to the generation of internal waves between two stratified layers.

A pycnocline refers to the region of a body of fluid where the rate of change of density is greatest. For a ship moving through a stratified fluid this refers to the thin plane that separates the two distinct layers. However, in the oceanic context the pycnocline is a large volume of water hundreds of metres deep that is characterised by a large increase in density with depth. This differentiates it from the mixed (surface) layer and deep layer where density distribution is largely constant. Depending on latitude and weather the pycnocline layer can be present at the ocean's surface, with no mixed layer present (Emerson et al. 2004). This results in a linearly stratified ocean surface with a gradually increasing density gradient. A linear stratification can still create internal waves and increased resistance as shown by Mercier et al. (2011).

It is possible for a thin pycnocline between two distinct layers to occur close to the ocean's surface under specific circumstances. A layer of warmer fresh water can be generated on top of colder sea water due to ice melting from a glacier or other similar processes (Grue 2018). This creates perfect conditions for the generation of internal waves if a moving body like a ship passes through this region. The dead water effect will create a large increase in resistance when a ship moves through this region with a speed close to the celerity of the internal waves being generated (Grue 2015).

The most frequent cause of naturally occurring dead water is runoff from melting glaciers depositing warmer, fresh water on top of oceanic salt water, particularly in fjord regions (Grue 2018). According to Mortensen et al. (2013) the pycnocline between fresh and salt water for a standard glacial fjord is only observed between 30 and 90 m during summer months and between 16 and 40 m in winter months. This results in a net change in minimum pycnocline depth (h_{min}) of 14 m and a net change in maximum pycnocline depth (h_{max}) of 50 m.

Johannesson et al. (1995) predict glacial mass changes between 5 and 10 m w.e. (metre water equivalent from summer to winter; a measure of the total volume of water lost divided by the surface area of the glacier, represents the 'depth' of water into the glacier that has melted from summer to winter). It is this change in glacial mass that results in the increase in pycnocline depth, due to the large amount of fresh water being deposited onto the ocean surface by the melting glacier. According to the climate forecast by Nesje et al. (2008) climate change could lead to a total glacial melting of up to 140 ± 30 m w.e. of ice by the year 2100. Due to the limited research performed in this area it is not possible to confidently say how exactly this increase in glacial melting will affect pycnocline depth, but it is foreseeable that pycnocline depth would increase.

2.2. Internal waves

In a stably stratified environment, any disturbances such as wind or the motion of a body within the fluid can create internal waves. These waves can occur for distinctly stratified or linearly stratified environments, such as within the oceanic pycnocline. Oceanic internal waves can travel over extremely long distances and can be observed from space, can be seen in Figure 1, both internal and atmospheric waves off the coast of Australia.

Internal waves can also be created much closer to the surface due to the motion of a body through a distinctly stratified region such as a one made up of fresh water sitting atop salt water. While internal waves create resistance in a manner similar to the wave making resistance of surface waves, they differ in several important ways. The difference in density between air and water is much larger than the difference in density between two strata of water. As a result of this surface waves will have a much larger restoring force (Esmaeilpour et al. 2018). This in turn means that internal waves have a larger amplitude and period but a smaller celerity.

2.3. The dead water effect

If a flow is known to be stably stratified due to the Brunt-Vaisala frequency and Richardson number, the key parameter in determining whether the dead water phenomenon will occur is the densimetric Froude number. The densimetric Froude number is defined as (Esmaeilpour 2017):

$$Fr_i = U/\sqrt{\frac{\Delta\rho}{\rho_0}gh} \qquad (3)$$

Where Fr_i is the densimetric (or internal) Froude number, U is the ship's velocity in m/s, $\Delta\rho/\rho_0$ is the relative density difference, and h is the reference pycnocline depth in m. The densimetric Froude number represents the ratio of ship speed to the celerity of the largest internal wave and as such the dead water phenomenon will occur when the densimetric Froude number is close to 1.

The dead water effect was first reported by Nansen and Sverdrup (1897) after his ship suddenly lost speed and steering while journeying to the North Pole. The phenomenon had been noted previously including as early as 98AD by Tacitus (98AD) who described a calm sea on which it was not possible to row a boat, however Nansen was the first to correctly identify its cause as the generation of internal waves in a stratified fluid. Ekman (1904) was the first researcher to conduct scientific research on the dead water phenomenon. He found experimental proof the dead water effect, simulating it using a scale model in a tank filled with a stratified fluid. The primary new development of Ekman's research was the discovery of a dispersive undulating depression that accompanies the stationary internal waves reported by Nansen. The resistance caused by this
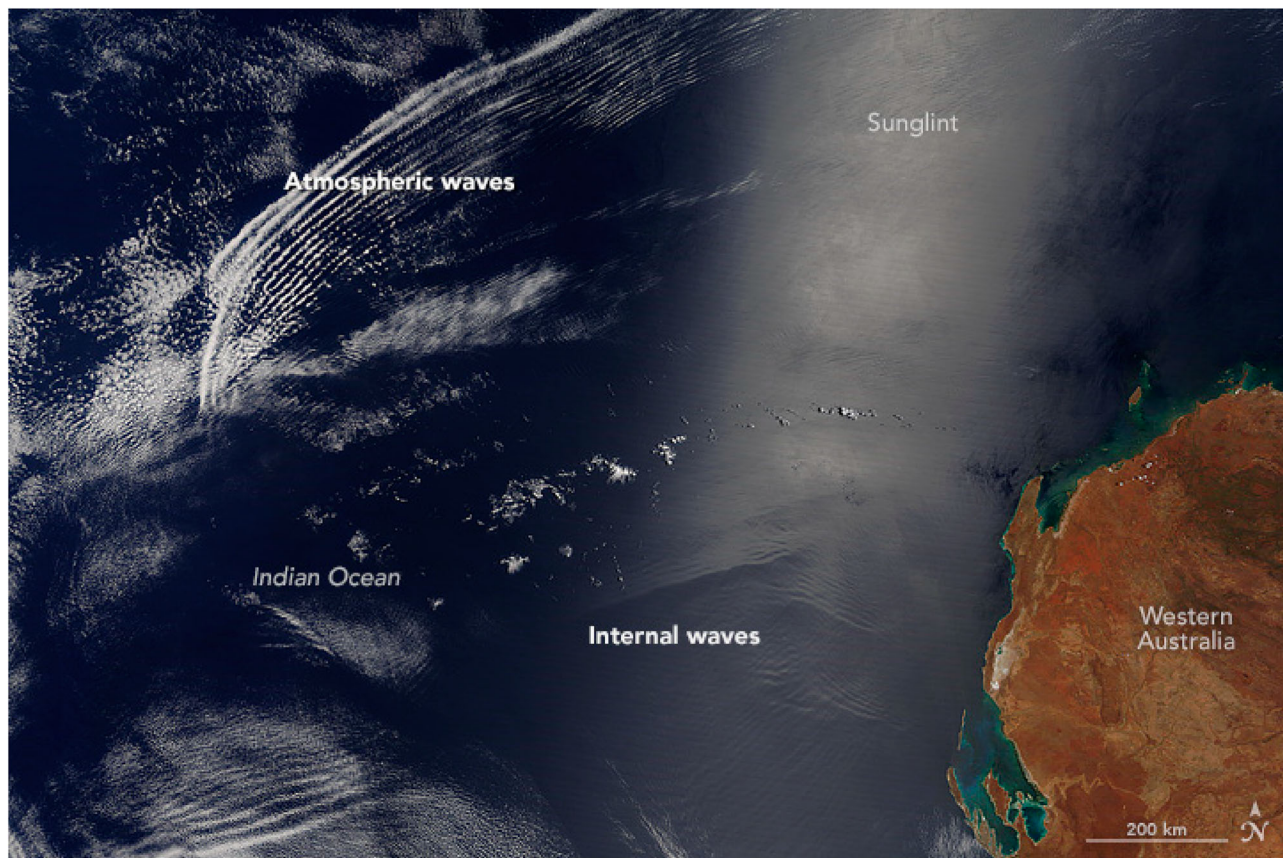
Figure 1. Satellite photo of internal waves off the coast of Australia (NASA 2016).

secondary phenomenon is known as Ekman wave-making drag to differentiate it from the effect of Nansen's stationary internal waves. It is these two effects acting concurrently that create the overall dead water effect.

Miloh et al. (1992) created the first mathematical model capable of simulating the dead water effect using linear theory. They simulated a ship as a prolate spheroid and found a sudden increase in wave resistance as the densimetric Froude number approached 1, proposing a theoretical explanation of the dead water effect. This provided a largely accurate model of the dead water effect and was able to predict both the internal wave pattern predicted by Nansen as well as the dispersive undulating depression that Ekman predicted. However, as the approach was based on linear potential flow theory it cannot consider the effects of turbulence and viscosity and is therefore unable to fully model the complexities of the flow.

Ekman's work was expanded by Mercier et al. (2011) by using modern techniques to perform a broader range of experiments including three-layer stratification as well as linear stratification. Linear stratification describes a case where there is a gradual density gradient across a large vertical distance. This is of particular interest as it occurs much more frequently in nature than stratification between two distinct fluids. Ekman's (1904) work was further expanded upon by Fourdrinoy et al. (2020), who investigated the cause and nature of Ekman wave-making drag. They demonstrated that Ekman wave-making drag is a result of the initial acceleration of the ship that occurs upon entering a region of dead water. A linear analytical model was also used to prove that the oscillating regime of the Ekman wave-making drag is only temporary and that a ship can escape this regime while maintaining constant propulsion.

Grue (2015) expanded the 2D theory proposed by Miloh et al. (1992) by creating a three-dimensional numerical model. Grue (2015) discovered that the resistance due to the dead water effect was independent of draft and varied only with densimetric Froude number. His study utilised a strongly non-linear potential flow method that was able to obtain more accurate results than those derived from linear theory, but the model was still ultimately irrotational and thus was subject to the associated assumptions.

Esmaeilpour et al. (2018) were the first to utilise CFD to simulate the dead water effect. This allowed for a more complete model that included viscous and free surface effects although only the near field flow was simulated. Their research was largely in agreement with previous numerical results, however an increase in the frictional resistance was also observed because of a thinning of the boundary layer around the hull due to the flow being partially constrained by the pycnocline. As this effect was caused by the boundary layer, which is a viscous effect, previous studies carried out using potential flow theory could not predict this increase in resistance. Later, Danieletto et al. (2019) compared the effects of dead water on both surface and submerged bodies by measuring their resistance in a towing tank. It was demonstrated that the resistance generated by internal waves was identical whether the body was partially or fully submerged. The present study builds on the previously reviewed CFD research by investigating the effect of dead water on modern containerships.

3. Case studies

All numerical modelling was carried out on the KRISO container ship (KCS) hull geometry due to the abundant experimental data and its widespread use in numerical studies. This allows partial

Table 1. KCS main particulars.

Property	Symbol	Unit	Full Scale	Model Scale
Scale factor	λ	–	1	31.599
Length	L	m	230	7.2786
Depth	D	m	19	0.6013
Draft	T	m	10.8	0.3418
Displacement	∇	m³	52030	1.649
Wetted surface area	S	m²	9530	9.5441
Block coefficient	C_b	–	0.651	0.651
Froude Number	Fr	–	0.26	0.26

validation of the results against a special subset of experiments performed in deep water and reported in Kim et al. (2001) in subsequent sections. The main particulars of the hull are given in Table 1.

The methodology adopted in this study was to validate the deep-water resistance value against the available experimental data. Then, the densimetric Froude number was varied by changing the depth of the pycnocline as well as the ship speed. Taking precedent from studies of shallow water ship hydrodynamics, the pycnocline depth to draft ratio (h/T) was varied between 0.25 and 10.5 to produce a range of cases. Additionally, two ship speeds, corresponding to Froude numbers of 0.26 (the service speed, 24 knots full-scale equivalent) and a lower speed corresponding to $Fr = 0.0431$ (4 knots full-scale equivalent) were modelled to create cases where $Fr_i < 1$. These case studies represent practical and extreme cases, to gauge the influence of varying operational conditions on the resistance of the hull. As mentioned in the previous section, a resistance spike is expected when $Fr_i \approx 1$. Case studies were therefore set to ensure these conditions are accounted for. The full test matrix is given in Table 2.

The full-scale equivalent pycnocline depths chosen varied from approximately 5.4 m to 113.4 m to cover the entire range of possible naturally occurring depths (0 m – 90 m) and to observe the effects of increasing pycnocline depths due to climate change (90 m – 113.4 m). While, as discussed in greater detail in the previous section, sufficient data does not yet exist to predict how much pycnocline depths are likely to increase by, an increase of more than 2 times the difference between summer and winter is assumed to be more than sufficient to account for a worst-case scenario.

The properties of fresh and salt water were taken from the International Towing Tank Conference (ITTC) (26th ITTC Specialist Committee 2011). Both were taken to have a temperature of 12°C

because, as explained in the following section, the Volume of Fluid (VoF) method used to model free surfaces requires a constant temperature (Siemens 2018). The density of fresh water, ρ_0, was taken as 999.5 kg/m³ and its dynamic viscosity, μ_0, was taken as 0.001234 Pa-s. The density of salt water, $\rho_0 + \Delta\rho$, was taken as 1026.64 kg/m3 and its dynamic viscosity, $\mu_0 + \Delta\mu$, was taken as 0.00136 Pa-s. A graphical representation of the general the setup used in this study is shown in Figure 2.

4. Numerical set up

The commercially available Reynolds Averaged Navier-Stokes solver, Star-CCM + was used to conduct all numerical modelling. The solver uses the finite volume method to discretise the governing equations into a finite number of adjoining control volumes.

4.1. Physics modelling

The turbulence model selected for the simulation was the standard k-ω model (Wilcox 2008). This was selected for its accuracy for low as well as high Reynold number flows and its relative computational economy. Terziev et al. (2019) found the k-ω model requires the least time per iteration of any two-equation eddy-viscosity turbulence model, making it a suitable choice for the present investigation.

As mentioned in the previous section, the VoF model was used to model the air—water interface and pycnocline. For the VOF method to be accurately applied the grid must be fine enough to capture the interface between fluids and the fluids must take up a large portion of the domain relative to their contact area (Siemens 2018). In addition, the VOF method assumes that the applied governing equations are valid for all present fluids and that all fluids have the same velocity, pressure and temperature. The result of this is that the governing equations can be solved for multiple fluids as though they were one, with distinctions between the fluids being accounted for by the differences in their volume fractions and phases.

The convective term in the Navier-Stokes equations was discretised using a second-order scheme. This removes the risk of the free surface 'smearing', which can occur for lower order schemes (Andrun et al., 2018). In addition, the segregated flow model was applied in the RANS solver for all simulations, solving the flow in

Table 2. Test matrix.

Ship Speed U (m/s)	Full-scale equivalent speed (kn)	Froude Number Fr	Reynolds Number Re	Pycnocline Depth h (m)	Depth to draft ratio h/T	Densimetric Froude Number Fr_i
0.366	4 kn	0.043	2.99×10^6	0.0855	0.25	2.4260
				0.1709	0.5	1.7155
				0.3418	1	1.2130
				0.5127	1.5	0.9904
				0.6836	2	0.8577
				0.8545	2.5	0.7672
				1.0254	3	0.7003
2.196	24 kn	0.26	1.795×10^7	No pycnocline[a]	-	-
				0.1709	0.5	10.293
				0.3418	1	7.2781
				0.5127	1.5	5.9426
				0.6836	2	5.1464
				0.8545	2.5	4.6031
				1.0254	3	4.2020
				1.5381	4.5	3.4310
				2.0508	6	2.9713
				2.5635	7.5	2.6576
				3.0762	9	2.4260
				3.5889	10.5	2.2461

[a]This case study is used for validation and verification in section 6.
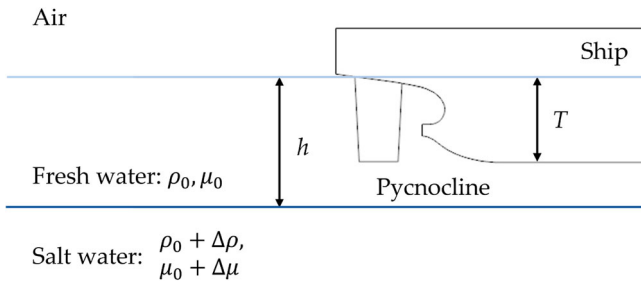
Figure 2 . Diagram of the set up used.

an uncoupled manner. The Semi-Implicit Method for Pressure Linked Equations (SIMPLE) algorithm was then utilised to find the overall solution procedure. To replicate the experimental results of Kim et al. (2001), the ship was fixed, in other words, running sinkage and trim were not accounted for.

4.2. Time step selection

The selected time step value follows previously conducted research by the authors. Specifically, the recommendation of Tezdogan et al. (2016) who set the time step as $\Delta t = 0.0035L/U$ was used. That recommendation was further tested in a variety of conditions and has been shown to deliver sufficiently accurate results (Elsherbiny et al. 2020; Terziev et al. 2021b, 2020, 2019a, 2019b, 2019c).

4.3. Computational domain

The computational domain dimensions and boundary conditions were selected based on recommendations of the (ITTC 2011). Specifically, the domain inlet is placed 1.5 ship lengths upstream of the forward perpendicular, where a velocity inlet boundary condition introduces the three fluids, separated at the predefined locations and with a speed equal but opposite that of the target ship speed as shown in Table 2. Air was introduced between $z = 0$, where the air–water interface is located, and the domain top. Fresh water was introduced between $z = 0$ and $z = -h$, while the space below $z = -h$ was occupied by salt water. The domain top was placed approximately 1.25 ship lengths from the undisturbed water surface, while the domain bottom and side were placed 2.5 ship lengths from the undisturbed water surface and centreline, respectively. The ship and domain centreline coincide, where a symmetry boundary condition was used to half the cell numbers and enable faster simulation run time. Finally, the pressure outlet was located 2.5 ship lengths downstream of the aft perpendicular, where the hydrostatic pressure was maintained. The domain and boundary conditions are depicted in Figure 3.

4.4. Mesh generation

The mesh was created using the automated meshing tool within STAR-CCM + . This utilises the cartesian cut-cell method and resulted in a mesh of approximately 2.9 million cells. The resulting mesh was primarily made up of unstructured hexahedral cells. There were also several areas of refinement within the mesh to ensure that the mesh was fine enough the accurately model complex flow features. Specifically, the areas immediately around the hull, in the wake pattern behind the hull, in the free surface and also around the pycnocline. This was done using local mesh refinements. The mesh at and around the hull is shown below in Figure 4, Figures
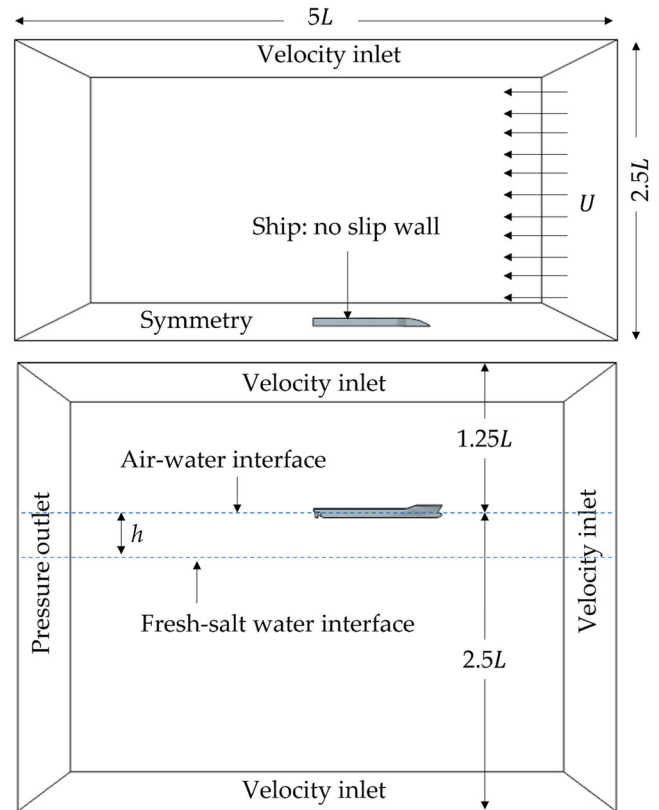

Figure 3 . Computational domain dimensions and boundary conditions.

5 and 6. The meshing strategy differs from a conventional ship resistance simulation by the fact that vertical gradients in the pycnocline must be resolved. Therefore, the free surface refinement is extended vertically to encompass the pycnocline at all h/T ratios as shown in Figure 6.

5. Results and discussion

As mentioned in the above sections, the main aim of this study is to investigate resistance changes as a result of flow stratification. Ship resistance coefficients are defined as:

$$C_{T,F,P} = 2R_{T,F,P}/(\rho_0 U^2 S) \qquad (4)$$

where $C_{T,F,P}$ and $R_{T,F,P}$ are the total (T), frictional (F), and pressure (P) resistance coefficient and force in Newtons, respectively. The resistance coefficient at $Fr = 0.26$ (the design speed) obtained by Kim et al. (2001) $C_{T,experiment} = 0.003557$ compares well with the numerically obtained value of 0.00350, with an absolute error of 0.544%. The resistance was very slightly over predicted; the relative agreement between the experiment and the CFD model discussed in previous sections is deemed sufficient. Unfortunately, no experimental results exist for the slower speed example so a comparison could not be made.

5.1. Resistance in a stratified fluid

Numerical simulations were performed at $U = 0.366 \, m/s$ for pycnocline depths ranging from $0.25 \leq h/T \leq 3$, resulting in densimetric Froude numbers of the range $0.7 \leq Fr_i \leq 2.426$; and also at $U = 2.196 \, m/s$ for pycnocline depth ranging from $0.5 \leq h/T \leq 10.5$, resulting in densimetric Froude numbers of the range $2.25 \leq Fr_i \leq 10.29$. The resistance coefficients for both speeds are
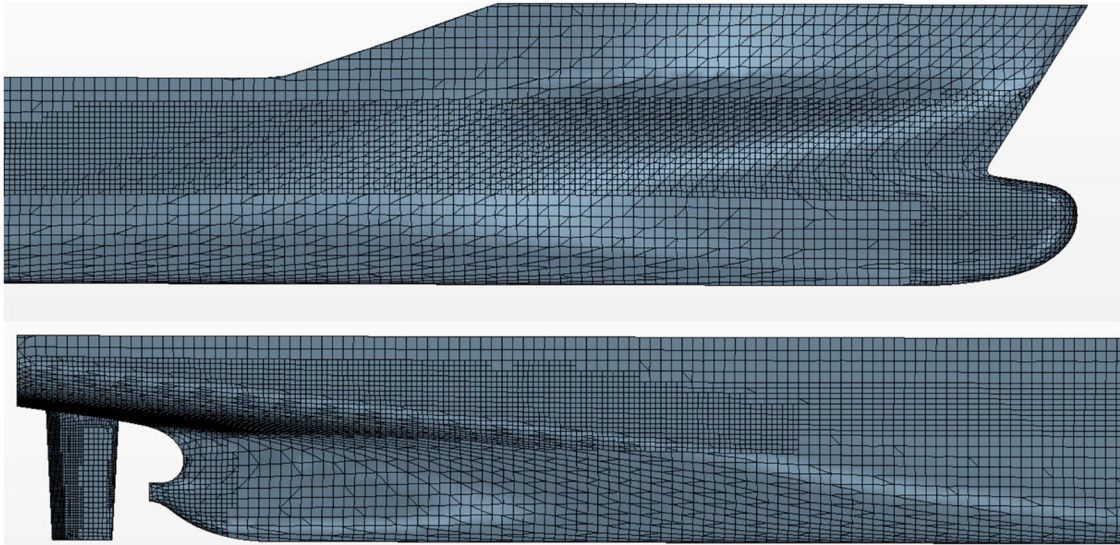
Figure 4 . Mesh on the surface of the KCS, used in all numerical simulations.

shown in Figure 7 along with the resistance coefficient of the homogeneous fluid at $U = 2.196\ m/s$ to act as a baseline.

Figure 7 shows that the total resistance coefficient peaks between $Fr_i = 0.858$ and $Fr_i = 0.99$. This is consistent with the results found by Miloh et al. (1992), who found that total resistance peaks at $Fr_i = 0.88$ using potential flow theory. Similarly, Figure 7 confirms the results of Esmaeilpour et al. (2018), who found the peak of resistance between $Fr_i = 0.83$ and $Fr_i = 0.91$ using CFD. The latter also reported the increase in resistance coefficient to be around 6 times higher than the resistance coefficient of the homogeneous case. This is consistent with our findings: the resistance coefficient at $U = 3.66$ m/s is predicted as 0.00454 for the homogeneous case compared to 0.02629; an increase of approximately 580%.

Figure 8 shows the numerically predicted total resistance coefficients as a function of pycnocline depth. The figure demonstrates that for the range of realistic pycnocline depths there is almost no

increase in resistance for a hull travelling at service speed. This is consistent with the findings of Esmaeilpour et al. (2018) which saw little to no increase in resistance for experiments with $Fr_i > 2$. Such results are analogous to those obtained for shallow water where the densimetric Froude number is replaced by the depth Froude number (Havelock 1908). The latter expresses the ratio of the wave celerity and ship speed, and as is the case in internal wavemaking, shallow water wavemaking peaks when the depth Froude number is approximately 1 (Benham et al. 2020; Terziev et al. 2020), as shown in Figure 7 and Figure 8 in the case of dead water.

5.2. Resistance decomposition

The total resistance coefficient is composed of frictional resistance and pressure resistance. The latter contains viscous pressure drag and wave drag (Molland et al. 2017). As shown previously, the
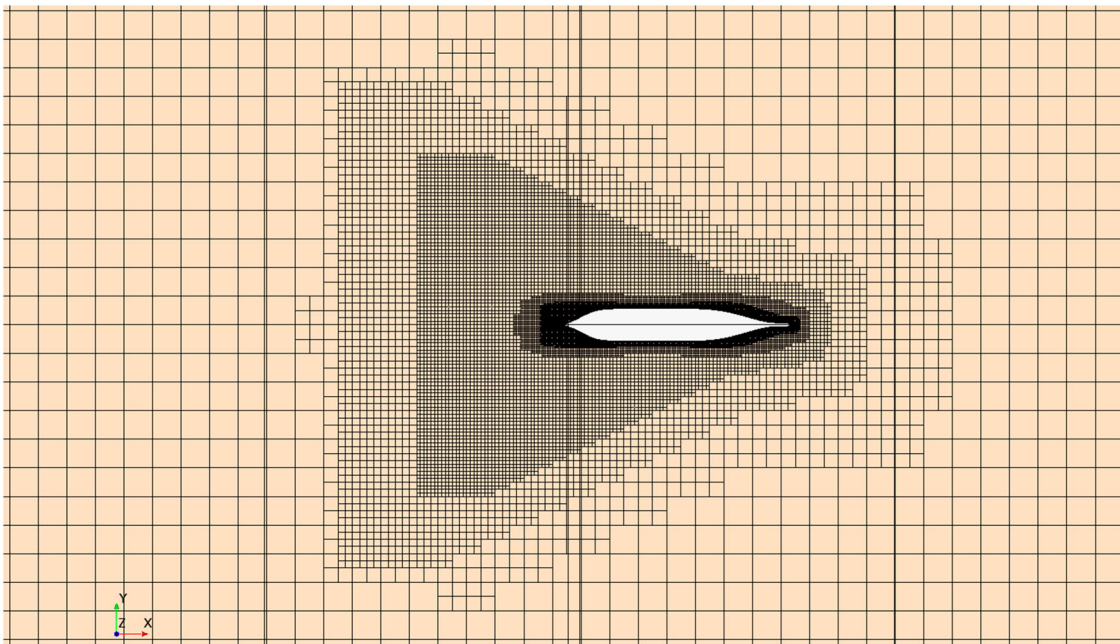

Figure 5. Mesh on the air-water interface, used for all numerical simulations. The mesh is mirrored about the central symmetry plane for visualisation purposes.
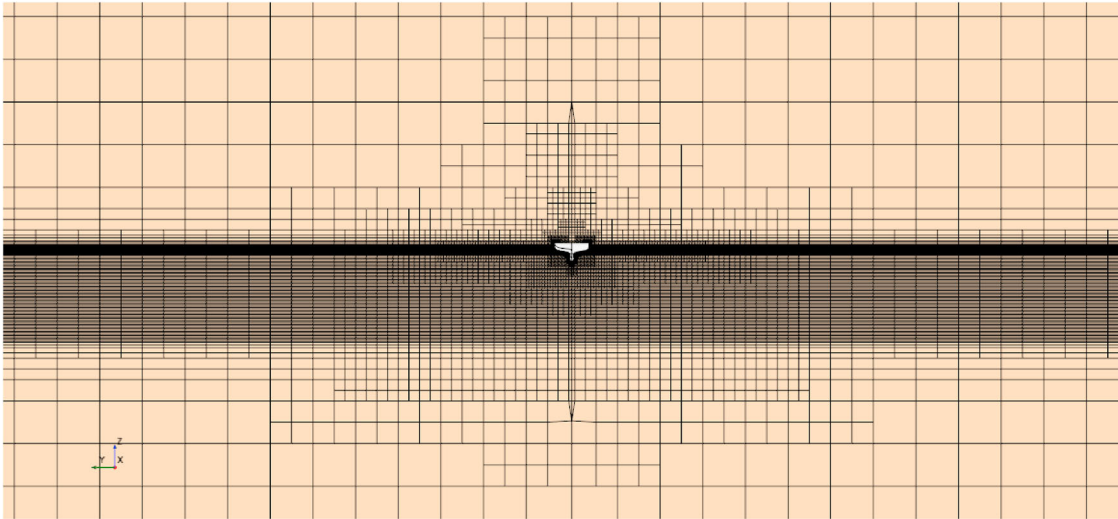
Figure 6. Front view of the mesh, showing the mesh refinement used to resolve the fresh-salt water interface and air-water interface. The mesh is mirrored about the central symmetry plane for visualisation purposes.

total resistance can vary considerably under certain conditions, but it is also important to show the reasons behind this increase. In other words, the distribution of frictional and pressure resistance coefficients is examined within this subsection.

Figure 9 shows the breakdown of the resistance coefficient into its shear resistance and pressure resistance components. It demonstrates that for example with little increase in total resistance (i.e. examples with a total resistance coefficient close to 0.005) shear effects are dominant, which is to be expected at such a low speed (Song et al. 2019; Terziev et al. 2021a). However for example with a large increase in resistance the pressure resistance is dominant. This is because the generation of internal waves, like conventional wave-making resistance, is a pressure effect. The

relative make-up of the total resistance coefficient is further analysed in Figure 10.

Figure 10 shows the relative make-up of the total resistance coefficient. In other words, it shows the relative importance of the frictional and pressure components under all conditions examined in this paper. Such an assessment is useful because it offers an intuitive framework for understanding the importance of each resistance component. Figure 10 demonstrates that under conditions where Fr_i is near unity, the balance of friction and pressure alters significantly. The frictional component takes approximately 90% for the low-speed case of 4knots when the desimentric Froude number is far from 1. However, this allocation is revered, with pressure resistance accounting for up to 80% of the total at
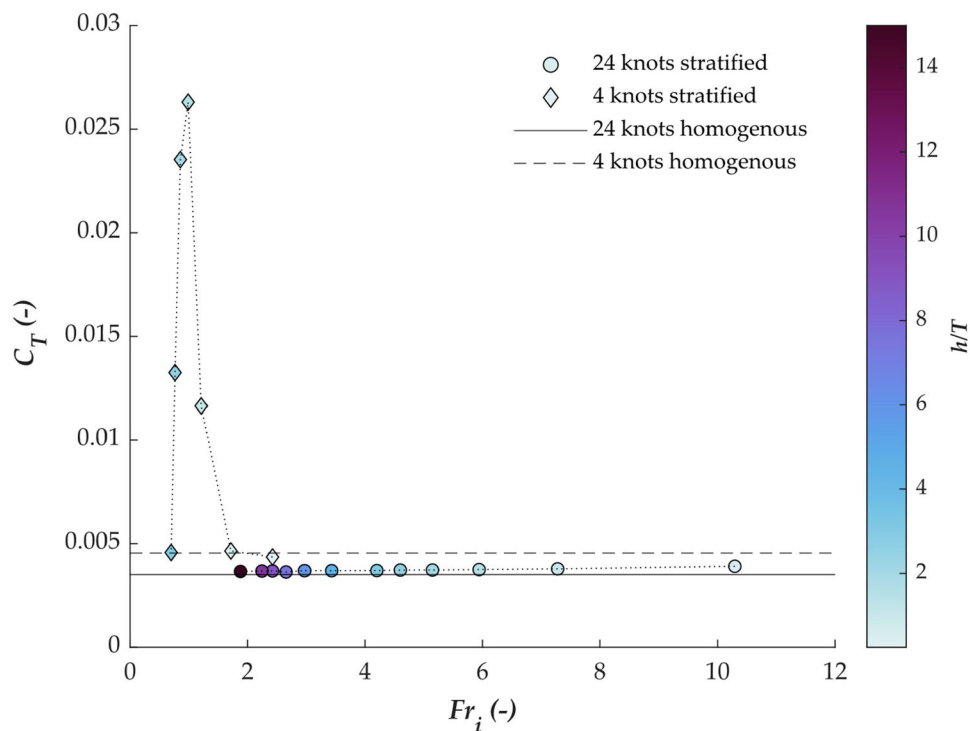

Figure 7. Total resistance coefficient against densimetric Froude number. Data is colour coded according to the dimensionless depth of the pycnocline.
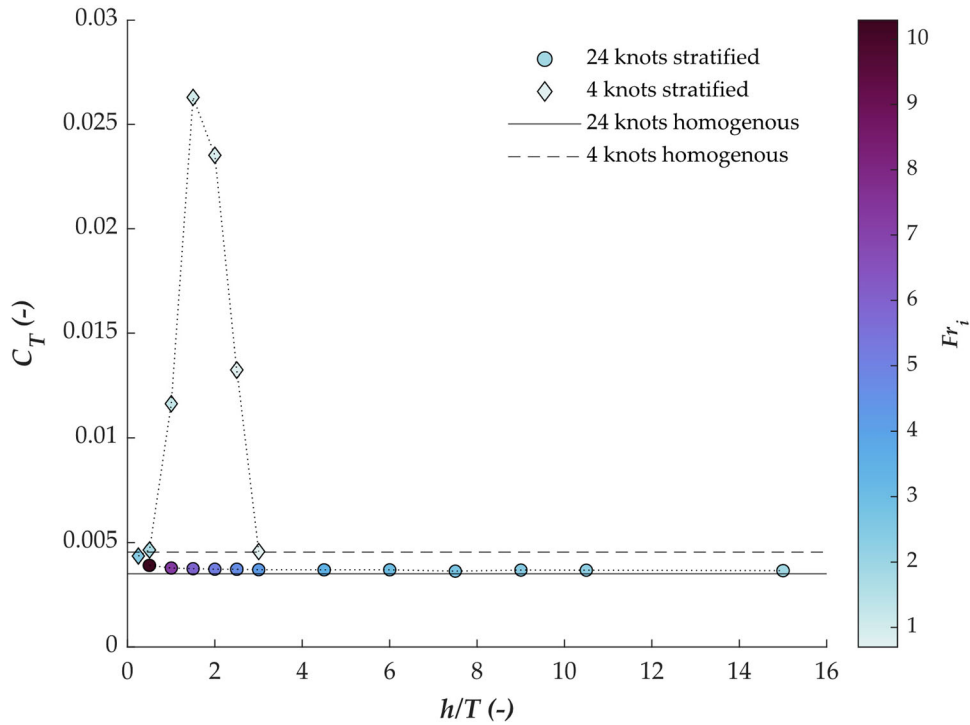
Figure 8. Total resistance coefficients as a function of the pycnocline depth-to-draft ratio.

$Fr_i = 0.99$. This shows the importance of considering all environmental phenomena and attempting to forecast any changes in the conditions a vessel will operate in. If an area is prone to flow stratification, the possibility of dead water must be considered during the design stage. For example, a relatively small reduction in speed or change in pycnocline depth, bringing the densimetric Froude number to 0.7 can reverse the majority of the increase in resistance.

It should be noted that in the high-speed case, the pressure resistance component grows in importance by approximately 5% from the cases when $Fr_i = 2.25$ to $Fr_i = 10.3$. The change in densimetric Froude number is driven by a vertical change of the pycnocline depth. Therefore, as shown in Table 2, the depth to pycnocline

draft ratio increases from 0.5–10.5. Although the relative increase in resistance coefficient is small, it cannot be neglected. In the aforementioned Fr_i range, the total resistance coefficient grows by 6.31%. To put that value into context, recent work on energy saving pre-swirl ducts showed less than 5% efficiency improvements (Andersson et al. 2022). Therefore, dead water effects must be considered regardless of whether the densimetric Froude number is near 1 because the resistance of the vessel is higher even if a hull operates far from $Fr_i = 1$. The cause for such an increase is the acceleration of flow in the top layer as a result of the limited available space between the hull and the salt-water interface. As discussed above, the restoring force of the internal wave system is much smaller than that of the air–water interface, but this restoring
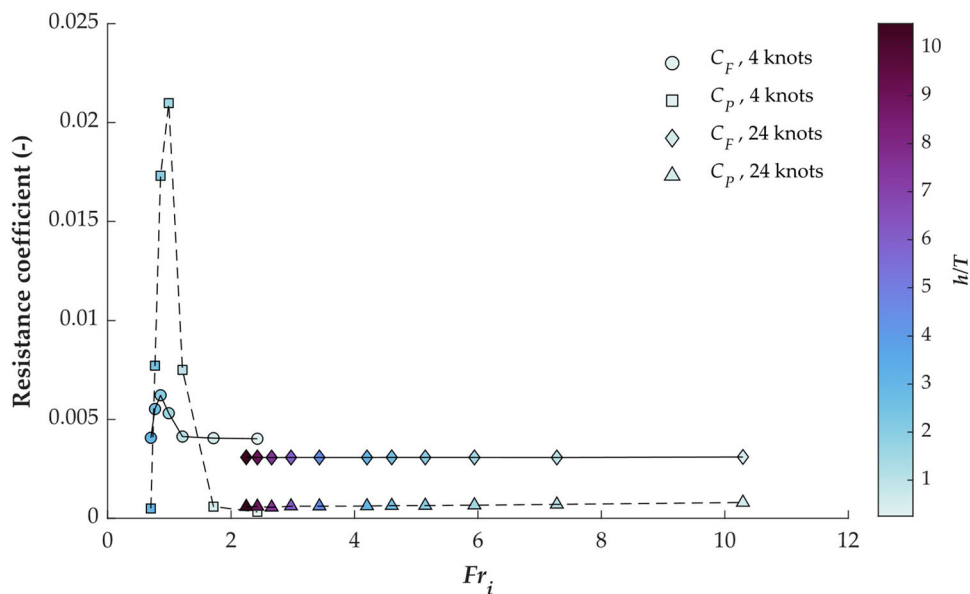

Figure 9. Pressure (C_P) and frictional (C_F) resistance coefficients obtained using CFD for all case studies.
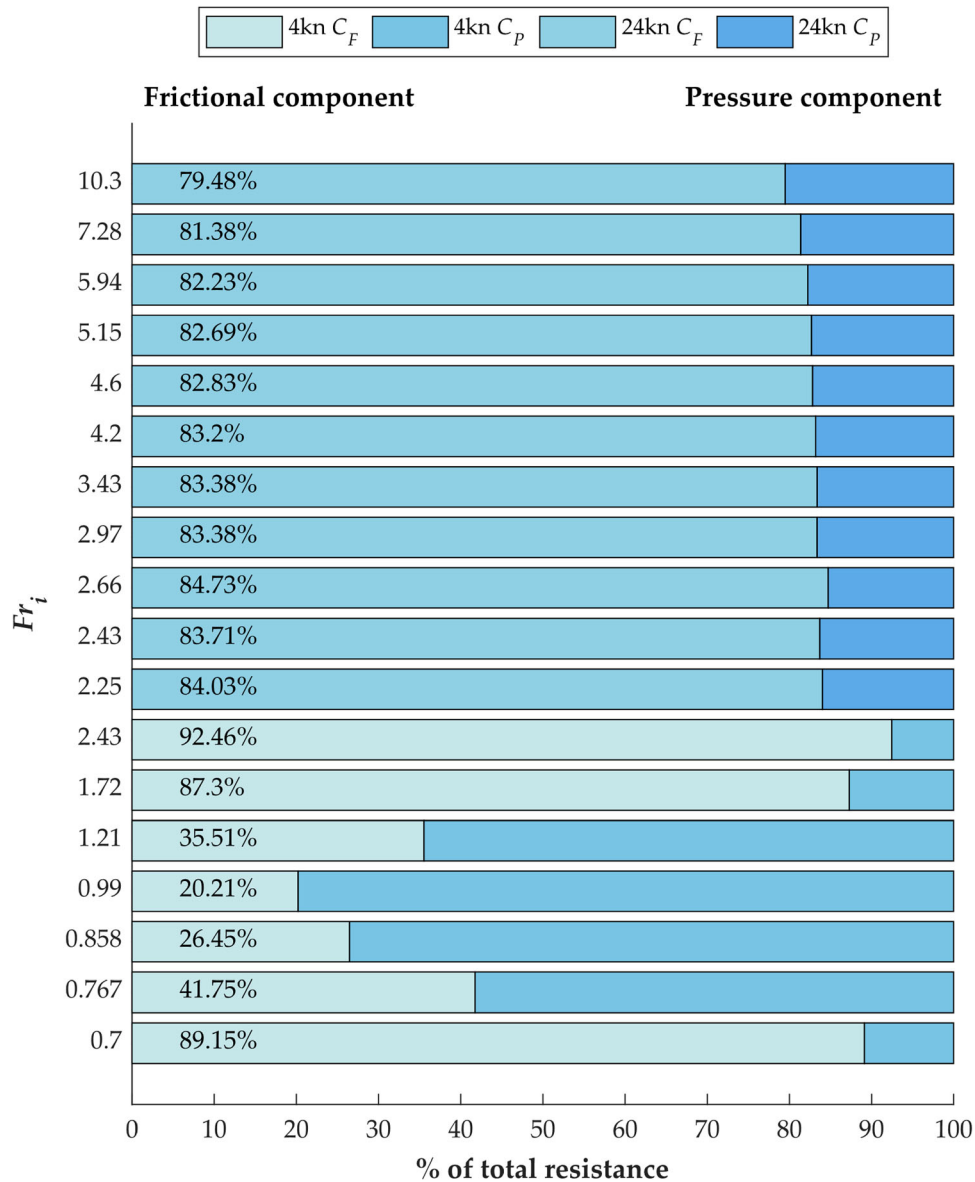
Figure 10. Relative make-up of the total resistance coefficient. Darker colours show the 24kn cases. Note that all 24 knot cases are grouped above the 4 knot cases and $Fr_i = 2.25$ corresponds to the 24 knot case shown in Table 2.

force is sufficiently strong to cause a measurable increase in resistance under any operational conditions.

5.3. Wave field

As discussed in previous sections, the presence of a fresh water-salt water interface modifies wave making considerably. The purpose of this subsection is to provide some visual aids in explaining the phenomenology of increase in resistance discussed previously. The first step is to compare the experimental wavecut data provided by Kim et al. (2001) with the numerical model used for this study to ensure accuracy of the wavefield. The comparison is shown in Figure 11, which shows excellent agreement between this study (labelled CFD) and the experiment (labelled EFD). The agreement deteriorates and breaks down at x/L = −1, where the mesh shown in Figure 5 coarsens. This has the dual purpose of reducing the cell count and eliminating waves before they reach the outlet, and as such, the divergence of results at this point is expected.

Figure 12 shows the internal wave making at $h/T = 1.5$ for the 24 knot case ($Fr_i = 5.94$) and the 4 knot case ($Fr_i = 0.99$). It is apparent that as the densimetric Froude number is approximately 1, the internal wave system resembles the wave front generated when a ship advances at the critical speed in shallow water. This phenomenon is produced only when the ship's speed is approximately equal to the celerity of waves. The internal wave system mirrors the air–water interface: wave crests at the bow become wave troughs when the speed is low. However, at the design speed, the depression observed at the parallel midbody is replicated in both free surfaces. In essence, the near-field disturbance produced by the hull is sufficiently strong to force fresh water between the vessel and the free surface, depressing the internal interface.

6. Validation and verification

A validation and verification study was undertaken to build confidence in the accuracy and robustness of the numerical model employed. This procedure is carried out for the case where
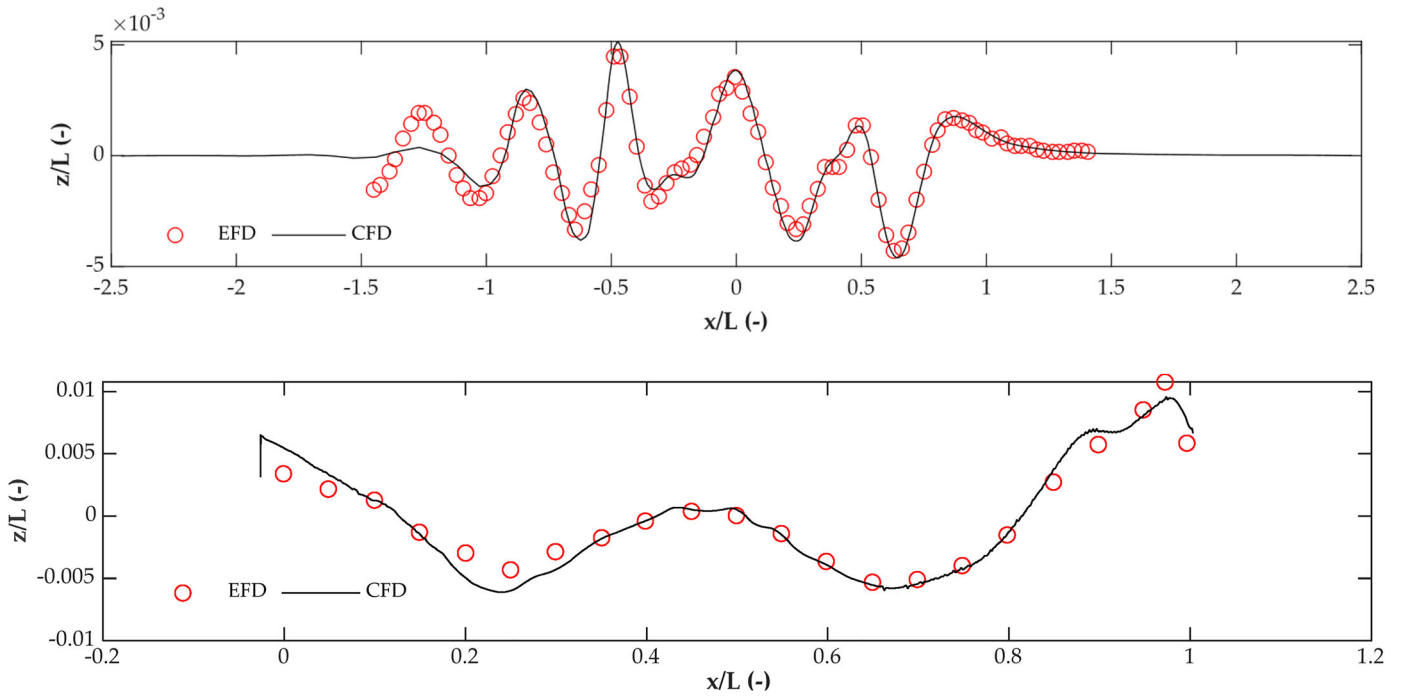
Figure 11. Comparison of experimental (EFD) and numerical (CFD) wavecut data for y/L = 0.1509 (top) and on wave elevation on the ship hull (bottom) at the design speed of 24 knots. The ship is located between 0 < x/L < 1.

experimental data is available, since that is a requirement in validating a solution (Roache 2009; Wilson et al. 2001). Experimental data is taken from Kim et al. (2001) for the deep water condition without a pycnocline.

Before validation can be attempted, the numerical uncertainty must be determined. In this study, the Grid Convergence Index, which relies on Richardson Extrapolation is used (Celik et al. 2008). The first step in the procedure is to create the so-called grid triplet, comprising the fine, medium, and coarse solution. Following recommendations of Burmester et al. (2020), the grid and time step are magnified by the same constant factor, known as the refinement factor (r), to ensure the Courant number is the same across all three solutions. As recommended by ASME (American Society of Mechanical Engineers 2009) and ITTC (2008), $r = \sqrt{2}$ is used. The resulting mesh numbers are given in Table 3. As mentioned previously, the time step of the fine simulation, $\Delta t = 0.0035 L/U$ is also multiplied by the same refinement factor.

Once the fine (f_1), medium (f_2), and coarse (f_3) solutions are produced, the numerical error may be estimated as shown in Eq. (3):

$$\delta = \varepsilon_{21}/(r^p - 1) \qquad (3)$$

where $\varepsilon_{21} = f_2 - f_1$, and p is the observed order of accuracy, defined as shown in Eq. (4) (Roache 1997):

$$p = \ln(|\varepsilon_{21}/\varepsilon_{32}|)/\ln(r) \qquad (4)$$

where $\varepsilon_{32} = f_3 - f_2$. Once these parameter are known, the numerical uncertainty may be predicted using:

$$GCI = 100(FS|\delta/f_1|) \qquad (5)$$

where $FS = 1.25$ is the Factor of Safety. The numerical uncertainty, GCI, and the experimental uncertainty, U_E, are used to predict the validation uncertainty:

$$U_V = \sqrt{GCI^2 + U_E^2} \qquad (6)$$

A numerical simulation is validated if the error $E = 100(f_1 - f_{exp})/f_{exp}$, with f_{exp} being the experimentally obtained value, is smaller than the validation uncertainty. The results of the validation and verification assessment for the case without a pycnocline listed in Table 2 are given in Table 4.

Table 4 shows that the difference between the medium and fine solution (ε_{21}) is smaller than the difference between the coarse and medium solution (ε_{32}), meaning that the numerical model exhibits monotonic convergence. Using the Grid Convergence Index methodology, the predicted numerical uncertainty is negligible. The numerical solution is also characterised by an error $E = 0.54\%$, showing good performance against the experimental result reported by Kim et al. (2001). Using the experimental uncertainty of 0.64%, reported in the experimental campaign, the solution is validated since the validation uncertainty is predicted as approximately 0.64%. This exercise demonstrates that numerical set up is able to accurately predict the resistance of the hull.

7. Conclusion

This paper investigated the effect of flow stratification on ship resistance using a commercially available RANS solver, Star-CCM + . Two speeds were used to produce a wide range of case studies, incorporating densimetric Froude numbers above and below 1 to capture all possible conditions a vessel may encounter.

The results showed a marked increase in resistance when the densimetric Froude number is approximately 1. This was linked to the mechanism driving the peak in resistance observed in confined waters when the depth Froude number is approximately 1, since in both cases, the celerity of the waves is equal to the ship speed. At the operational speeds of modern containerships, taken as 24 knots for the KCS, flow stratification creates an increase in resistance of approximately 6%. Such an increase may be a significant difference if the operational area of a vessel is prone to flow stratification. Conversely, when the densimetric Froude
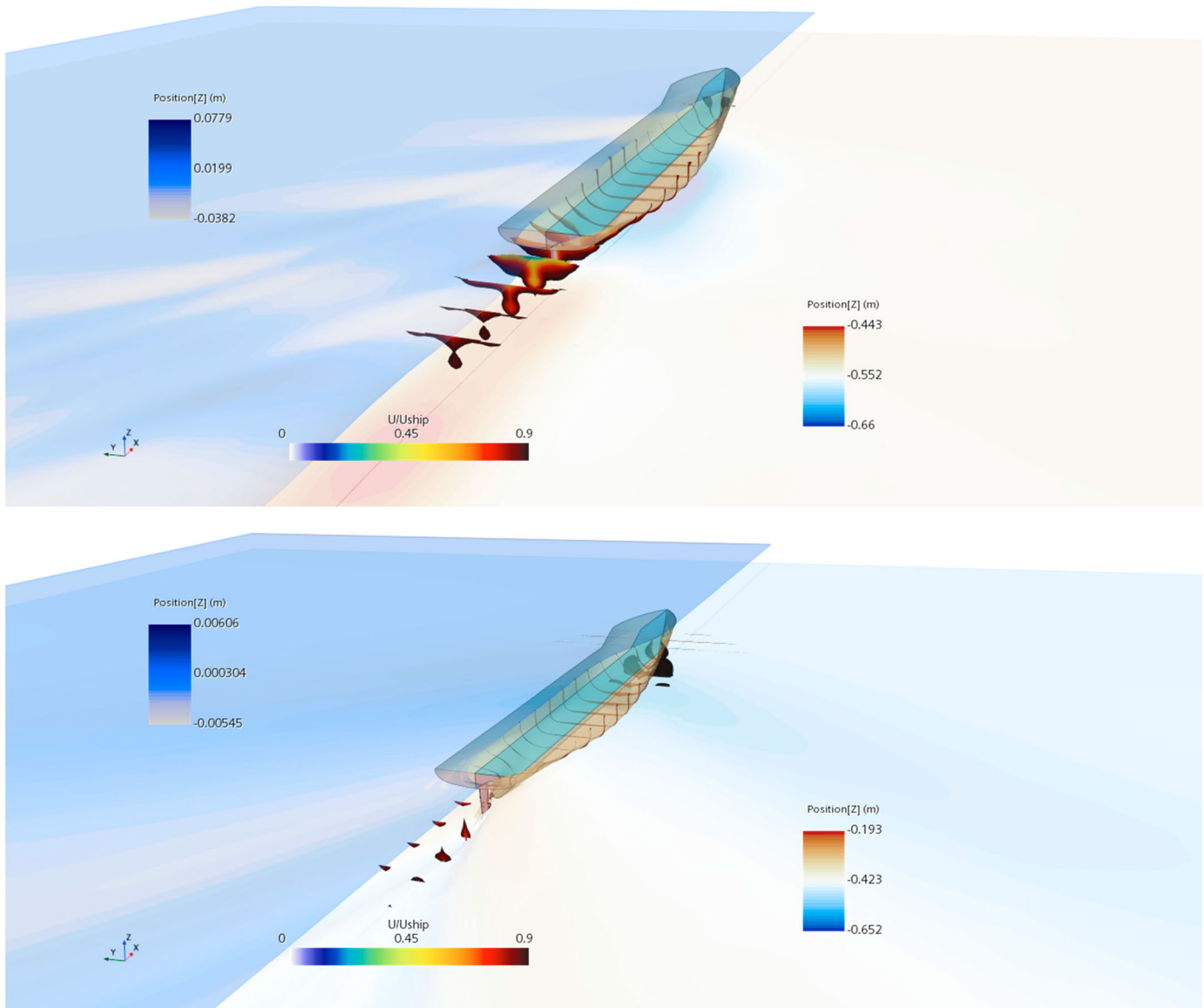
Figure 12. Wave-making and boundary layer shed by the ship at 24 knots (top) and 4 knots (bottom). In both cases, $h/T = 1.5$, but $Fr_i = 5.94$ in the top figure and $Fr_i = 0.99$ in the bottom figure. The lefthand side shows the air-water interface, while the righthand side depicts the mirrored internal free surface. The boundary layer velocity distributions are depicted in dimensionless form.

number is close to 1, the increase in the resistance is approximately six-fold, confirming results obtained by other researchers.

Unlike potential flow studies, this work accounted for viscous effects and therefore friction. The results show that, as expected, at low speeds friction makes up about 90% of the total resistance. In the presence of dead water, the pressure resistance spikes and makes up approximately 80% of the total resistance at the same speed. This highlights the importance of taking into account the operational conditions of the hull fully.

The present study may be extended in a variety of ways. Firstly, running sinkage and trim were not considered to match the experimental campaign. However, it is expected that the presence of dead

water may impact the dynamic attitude of the hull and may compromise trim optimisation carried out for homogenous flows. Alternatively, the action of the propeller is known to impact the flow field considerably, making it an interesting addition. Experiments are also necessary to provide validation data for the dead water phenomenon.

Table 4. Validation and verification exercise results.

Property	Symbol	Value	Unit
Fine solution	f_1	40.7424	N
Medium solution	f_2	40.7450	N
Coarse solution	f_3	41.0892	N
Refinement ratio	r	$\sqrt{2}$	-
Error	δ	1.95E-05	-
GCI Uncertainty	GCI	5.98E-05	%
Experimental uncertainty	U_E	0.64	%
Validation uncertainty	U_V	0.64	%
Experimental Value	f_{exp}	40.965	N
Comparison error	E	0.5444	%
Solution validated?	**Yes**		

Table 3. Mesh numbers used for the fine, medium and coarse simulations.

Mesh	Cell Count (N)
Fine	2907830
Medium	1493854
Coarse	726107

Acknowledgements

Disclosure statement

No potential conflict of interest was reported by the author(s).

ORCID

Momchil Terziev http://orcid.org/0000-0002-1664-6186
Tahsin Tezdogan http://orcid.org/0000-0002-7032-3038
Atilla Incecik http://orcid.org/0000-0001-6584-6320

References

26th ITTC Specialist Committee. 2011. Fresh Water and Seawater Properties. Int. Towing Tank Conf. 5, 1596–1599. https://doi.org/10.1002/cphc.200400116.

Andersson J, Shiri AA, Bensow RE, Yixing J, Chengsheng W, Gengyao Q, Deng G, Queutey P, Xing-Kaeding Y, Horn P, et al. 2022. Ship-scale CFD benchmark study of a pre-swirl duct on KVLCC2. Appl. Ocean Res. 123:103134. doi:10.1016/j.apor.2022.103134.

Andrun M, Blagojević B, Bašić J. 2018. The influence of numerical parameters in the finite-volume method on the wigley hull resistance. Proc. Inst. Mech. Eng. Part M J. Eng. Marit. Environ. 233(4):1123–1132. doi:10.1177/1475090218812956.

[ASME] American Society of Mechanical Engineers. 2009. Standard for Verification and Validation in Computational Fluid Dynamics and Heat Transfer - ASME V&V 20-2009, ASME International.

Benham GP, Bendimerad R, Benzaquen M, Clanet C. 2020. Hysteretic wave drag in shallow water. Phys. Rev. Fluids. 5:64803. doi:10.1103/physrevfluids.5.064803.

Burmester S, Vaz G, el Moctar O. 2020. Towards credible CFD simulations for floating offshore wind turbines. Ocean Eng. 209:107237. doi:10.1016/j.oceaneng.2020.107237.

Celik IB, Ghia U, Roache PJ, Freitas C. 2008. Procedure for estimation and reporting of uncertainty Due to discretization in CFD applications. J. Fluids Eng. 130:078001. doi:10.1115/1.2960953.

Danieletto M, Brown JM, Radko T. 2019. The immortal science of dead water: effects of internal wave drag on propagating submerged bodies. J. Oceanogr. Mar. Res. 07:1–7. doi:10.35248/2572-3103.19.7.191.

Drazin PG. 1970. Kelvin–helmholtz instability of finite amplitude. J. Fluid Mech. 42:321–335. doi:10.1017/S0022112070001295.

Ekman VW.. 1904. On dead water. In: Nansen F, editor. Norwegian north polar expedition 1893–1896. Longmans, Green and Co; p. 1–150.

Ellingsen S, Brevik I. 2014. How linear surface waves are affected by a current with constant vorticity. Eur. J. Phys. 35. doi:10.1088/0143-0807/35/2/025005.

Elsherbiny K, Terziev M, Tezdogan T, Incecik A, Kotb M. 2020. Numerical and experimental study on hydrodynamic performance of ships advancing through different canals. Ocean Eng. 195:1–17. doi:10.1016/j.oceaneng.2019.106696.

Emerson S, Watanabe YW, Ono T, Mecking S. 2004. Temporal trends in apparent oxygen utilization in the upper pycnocline of the north pacific: 1980-2000. J. Oceanogr. 60:139–147. doi:10.1023/B:JOCE.0000038323.62130.a0.

Esmaeilpour M. 2017. A ship advancing in a stratified fluid: the dead water effect revisited [PhD thesis] University of Iowa. doi:10.17077/etd.5z2auqsl.

Esmaeilpour M, Ezequiel Martin J, Carrica PM. 2018. Computational fluid dynamics study of the dead water problem. J. Fluids Eng. Trans. ASME. 140:1–8. doi:10.1115/1.4037693.

Fourdrinoy J, Dambrine J, Petcu M, Pierre M, Rousseaux G. 2020. The dual nature of the dead-water phenomenology: nansen versus ekman wave-making drags. Proc. Natl. Acad. Sci. 117:201922584. doi:10.1073/pnas.1922584117.

Gill AE. 1982. Adjustment under gravity of a density-stratified fluid. Atmos. Dyn. 117–188.

Grue J. 2015. Nonlinear dead water resistance at subcritical speed. Phys Fluids. 27:1–16. doi:10.1063/1.4928411.

Grue J. 2018. Calculating FRAM's dead water. In: Arias AH, editor. The ocean in motion. Cham: Springer; p. 41–53.

Havelock T. 1908. The propagation of groups of waves in dispersive media, with aplication to waves on water produced by a travelling disturbance. proc. R. Soc. London. Ser. A. Contain. Pap. A. Math. Phys. Character. 81:389–430. doi:10.1098/rspa.1933.0074.

ITTC. 2008. Uncertainty Analysis in CFD Verification and Validation Methodology and Procedures. 25th ITTC 2008, Resist. Comm. 12.

ITTC. 2011. Recommended Procedures and Guidelines: Practical Guidelines for Ship CFD. 26th Int. Towing Tank Conf.

Johannesson T, Sigurdsson O, Laumann T, Kennett M. 1995. Degree-day glacier modelling with applications to glaciers in Iceland, Norway and Greenland. J. Glaciol. 41:345–358.

Kim WJ, Van SH, Kim DH. 2001. Measurement of flows around modern commercial ship models. Exp Fluids. 31:567–578. doi:10.1007/s003480100332.

Li Y, Smeltzer BK, Ellingsen S. 2019. Transient wave resistance upon a real shear current. Eur. J. Mech. B/Fluids. 73:180–192. doi:10.1016/j.euromechflu.2017.08.012.

Mercier MJ, Vasseur R, Dauxois T. 2011. Resurrecting dead-water phenomenon. Nonlinear Process. Geophys. 18:193–208. doi:10.5194/npg-18-193-2011.

Miloh T, Tulin MP, Zilman G. 1992. Dead-water effects of a ship moving in stratified seas. J. Offshore Mech. Arct. Eng. 115(2):105–110.

Molland AF, Turnock SR, Hudson DA. 2017. Components of hull resistance, in: ship resistance and propulsion: practical estimation of ship propulsive power, pp. 12–69. Cambridge: Cambridge University Press. doi:10.1017/9781316494196.005.

Mortensen J, Bendtsen J, Motyka RJ, Lennert K, Truffer M, Fahnestock M, Rysgaard S. 2013. On the seasonal freshwater stratification in the proximity of fast-flowing tidewater outlet glaciers in a sub-Arctic sill fjord. J. Geophys. Res. Ocean. 118:1382–1395. doi:10.1002/jgrc.20134.

Nansen F, Sverdrup O. 1897. Farthest North (Archibald Constable, 1897). Vol. 1.

Nappo CJ. 2012. International geophysics: The linear theory. Vol. 102. Academic Press; p. 29–56.

NASA. 2016. Waves Above and Below the Water. Image by Jeff Schmaltz [WWW Document]. Eath Obs. URL https://earthobservatory.nasa.gov/images/87519/waves-above-and-below-the-water.

Nesje A, Bakke J, Dahl SO, Lie Ø, Matthews JA. 2008. Norwegian mountain glaciers in the past, present and future. Glob Planet Change. 60:10–27. doi:10.1016/j.gloplacha.2006.08.004.

Roache PJ. 1997. Quantification of uncertainty in computational fluid dynamics. Annu. Rev. Fluid Mech. 29:123–160. doi:10.1146/annurev.fluid.29.1.123.

Roache PJ. 2009. Perspective: validation—what does It mean? J. Fluids Eng. 131:034503. doi:10.1115/1.3077134.

Sallée JB, Pellichero V, Akhoudas C, Pauthenet E, Vignes L, Schmidtko S, Garabato AN, Sutherland P, Kuusela M. 2021. Summertime increases in upper-ocean stratification and mixed-layer depth. Nature. 591:592–598. doi:10.1038/s41586-021-03303-x.

Schnelle KB. 2003. Atmospheric diffusion modeling. encyclopedia of physical. Elsevier; p. 679–705.

Siemens. 2018. Star-CCM+ User Guide version 13.04.

Song S, Demirel YK, Atlar M. 2019. An investigation into the effect of biofouling on the ship hydrodynamic characteristics using CFD. Ocean Eng. 175:122–137. doi:10.1016/j.oceaneng.2019.01.056.

Tacitus, 98AD. Germania.

Terziev M, Tezdogan T, Demirel YK, Villa D, Mizzi S, Incecik A. 2021a. Exploring the effects of speed and scale on a ship's form factor using CFD. Int. J. Nav. Archit. Ocean Eng. 13:147–162. doi:10.1016/j.ijnaoe.2020.12.002.

Terziev M, Tezdogan T, Incecik A. 2019a. Application of eddy-viscosity turbulence models to problems in ship hydrodynamics. Ships Offshore Struct. 15 (5):511–534. doi:10.1080/17445302.2019.1661625.

Terziev M, Tezdogan T, Incecik A. 2019c. A geosim analysis of ship resistance decomposition and scale effects with the aid of CFD. Appl. Ocean Res. 92:1–17.

Terziev M, Tezdogan T, Incecik A. 2019d. Influence of mixed flows on ship hydrodynamics in dredged channels. Proceedings of the International Conference on Offshore Mechanics and Arctic Engineering - OMAE. doi:10.1115/OMAE2019-95445.

Terziev M, Tezdogan T, Incecik A. 2020. Modelling the hydrodynamic effect of abrupt water depth changes on a ship travelling in restricted waters using CFD. Ships Offshore Struct. 16(10):1087–1103. doi:10.1080/17445302.2020.1816731.

Terziev M, Tezdogan T, Incecik A. 2021b. A numerical assessment of the scale effects of a ship advancing through restricted waters. Ocean Eng. 229:108972. doi:10.1016/j.oceaneng.2021.108972.

Tezdogan T, Incecik A, Turan O. 2016. A numerical investigation of the squat and resistance of ships advancing through a canal using CFD. J. Mar. Sci. Technol. 21:86–101. doi:10.1007/s00773-015-0334-1.

Walker JM. 1991. Farthest north, dead water and the ekman spiral. part 2: invisible waves and a New direction in current theory. Weather. 46:158–164.

Wilcox DC. 2008. Formulation of the k-w turbulence model revisited. AIAA J. 46:2823–2838. doi:10.2514/1.36541.

Wilson RV, Stern F, Coleman HW, Paterson EG. 2001. Comprehensive approach to verification and validation of CFD simulations—part 2: application for rans simulation of a cargo/container ship. J. Fluids Eng. Trans. ASME. 123:803–810. doi:10.1115/1.1412236.

Wüest A, Lorke A. 2003. Small-scale hydrodynamics in lakes. Annu. Rev. Fluid Mech. 35:373–412. doi:10.1146/annurev.fluid.35.101101.161220.